STUDY OF THE EFFECTS OF NUMERICAL MODEL ENHANCEMENTS FOR AEROSTRUCTURAL ANALYSIS IN TRANSONIC FLOWS

J Allan A. Lyrio[1], João Luiz F. Azevedo[2], Domingos A. Rade[1], Ricardo G. da Silva[2] & Carlos Breviglieri[3]

[1]Instituto Tecnológico de Aeronáutica, DCTA/ITA, São José dos Campos, SP, Brazil
[2]Instituto de Aeronáutica e Espaço, DCTA/IAE/ALA, São José dos Campos, SP, Brazil
[3]Embraer S.A., São José dos Campos, SP, Brazil

Abstract

The objective of the present work is to discuss the effects of model enhancements on the capability of performing static aeroelastic analyses of aeronautical configurations. The model improvements addressed in this effort concern the use of finer aerodynamic grids, different turbulence models and the size of the modal base for the representation of the structural deflection solution. The study considers the NASA Common Research Model (CRM), from the 6th AIAA CFD Drag Prediction Workshop, and the High Reynolds Number Aerostructural Dynamics (HIRENASD) configuration, from the 1st AIAA Aeroelastic Prediction Workshop. A clear improvement in the aerodynamic prediction of drag, pitching moment and pressure coefficient distributions is observed for the NASA CRM case. For the HIRENASD test case, aerodynamic grid refinement has yielded results that demonstrate the robustness of the developed fluid-structure interaction process.

Keywords: Static Aeroelasticity, Computational Fluid Dynamics, HIRENASD, NASA CRM, Radial Basis Functions.

1. Introduction

During the last years, the Computational Aerodynamics Group from the Institute of Aeronautics and Space, in DCTA/IAE/ALA, is working on the development, integration and validation of a fluid-structure analysis process for wing-fuselage configurations in typical commercial aircraft flight regimes [2, 3]. The use of lightweight materials in primary structures of aircraft with this type of geometry, and under the high dynamic pressure conditions of transonic flows, cause changes in aircraft shape and, therefore, the aerodynamic response also changes. Hence, accurate flight mechanics and structural load predictions require fluid-structure coupled numerical simulations to determine the aerodynamics of a configuration in aeroelastic equilibrium as described in Ref. [1]. Therefore, this present work shows a compilation of the most recent results of this process which still focuses on a level of structural flexibility equivalent to the wind tunnel models with high aspect ratio and swept wings, however, considering current practical CFD grid refinement for both aerodynamic and aerostructural analyses. The NASA's Common Research Model (CRM), Ref. [4], from the 6th AIAA CFD Drag Prediction Workshop (DPW), Ref. [5], are one of the geometries to be used here. Previously, the authors considered a Computational Fluid Dynamics (CFD) grid with 5 million cells. And now, it is simulated here considering 45 million CFD cells, as proposed in Test Case 5 of the 6th DPW [5]. Additionally, in order to verify the robustness of the solid mechanics modeling, two different sizes of structural modal basis are considered, with 16 and 34 flexible modes.

For the High Reynolds Number Aerostructural Dynamics (HIRENASD), Ref. [6], from the 1st AIAA Aeroelastic Prediction Workshop (AePW-1), three levels of CFD grid are used here for both aerodynamic and structural analyses with Menter Shear Stress Transport (SST) turbulence model. For the finer grid, the Spalart Allmaras (SA) turbulence model is also considered in order to have more comparable data with respect to what is reported in the literature for the HIRENASD model.

The next chapters present a summary of the developed methodology and implemented process followed by a extensive analysis of results in terms of wing deflections, pressure distribution and integrated aerodynamic coefficients. All these results consolidate the BRU3D-FSI process in static aerostructural analysis for tunnel models in wing-fuselage configurations.

2. Theoretical and Numerical Formulation

The following sections briefly describe the theoretical formulations used for aerodynamic and structural modeling, as well as the scheme used for load and displacement transfer between these two domains. The integration of all of these modules to perform the static aeroelastic process until equilibrium is, then, presented.

2.1 Aerodynamic Modeling

The aerodynamic calculations are performed using the in-house BRU3D code [7]. The code is based on the 3-D compressible Reynolds-Averaged Navier-Stokes (RANS) equations, that filter the fluctuating part of the fluid properties, treated via turbulence models, and maintain only the mean contribution of the flow. These equations are presented in Ref. [8] in their dimensional form as

$$\frac{\partial \mathbf{Q}}{\partial t} + \nabla.(\mathbf{E}_e - \mathbf{E}_v) = 0 \ . \tag{1}$$

The vector of conserved quantities, $\mathbf{Q}$, is given by

$$\mathbf{Q} = [\rho \ \rho u \ \rho v \ \rho w \ e \ \rho \tau_1 \ \rho \tau_2]^T \ . \tag{2}$$

Here, ρ is the density, u, v, w are the velocity vector components in Cartesian coordinates, e is the total energy per unit volume and p is the static pressure. Moreover, $\mathbf{E}_e$ and $\mathbf{E}_v$ are, respectively, the inviscid and viscous flux vectors, given by

$$\mathbf{E}_e = \begin{bmatrix} \rho \mathbf{V} \\ (\rho u \mathbf{V} + p\hat{i}_x) \\ (\rho v \mathbf{V} + p\hat{i}_y) \\ (\rho w \mathbf{V} + p\hat{i}_z) \\ (e + p)\mathbf{V} \\ \tau_1 \mathbf{V} \\ \tau_2 \mathbf{V} \end{bmatrix} \quad , \quad \mathbf{E}_v = \begin{bmatrix} 0 \\ (\tau_{xi}^l + \tau_{xi}^t)\hat{i}_i \\ (\tau_{yi}^l + \tau_{yi}^t)\hat{i}_i \\ (\tau_{zi}^l + \tau_{zi}^t)\hat{i}_i \\ (\beta_i^l + \beta_i^t)\hat{i}_i \\ \mu_{diff_1}\tau_{1,i}\hat{i}_i \\ \mu_{diff_2}\tau_{2,i}\hat{i}_i \end{bmatrix} \quad , \tag{3}$$

with

$$\beta_i = \tau_{ij}u_j - q_{Hi} \ . \tag{4}$$

In the previous equations, the dynamic viscosity coefficient from the viscous stress tensor is determined via Sutherland's formula. As also indicated in Ref. [7], the code solves the equations in an unstructured, cell-centered, conservative finite-volume formulation. Advective flux terms are computed using the 2nd-order Roe upwind scheme and cell-face viscous derivatives are obtained using the Green-Gauss theorem with corrections in the cell-face normal gradient components.

In addition to the Menter Shear Stress Transport (SST) turbulence model, already used in the previous work, the Spalart Allmaras (SA) turbulence model is also used here as implemented and described in Ref. [8]. The SA model is widely used by the aerospace community and is reported in the literature in HIRENASD model simulations for comparative study with experimental results from the AePW as described in Ref. [6].

2.1.1 NASA CRM Aerodynamic Model

The NASA Common Research Model wing-body configuration geometry was used as the optional test case 5, called "Coupled Aero-Structural Simulation", for the 6th AIAA CFD Drag Prediction Workshop. Therefore, the fluid mesh used here follows the same approach applied in Ref. [10], consisting in a block-structured hexahedral volumetric grid with quadrilateral surface mesh as shown in Fig. 1. Table 1 contains the grid sizes used here for the NASA CRM test case.
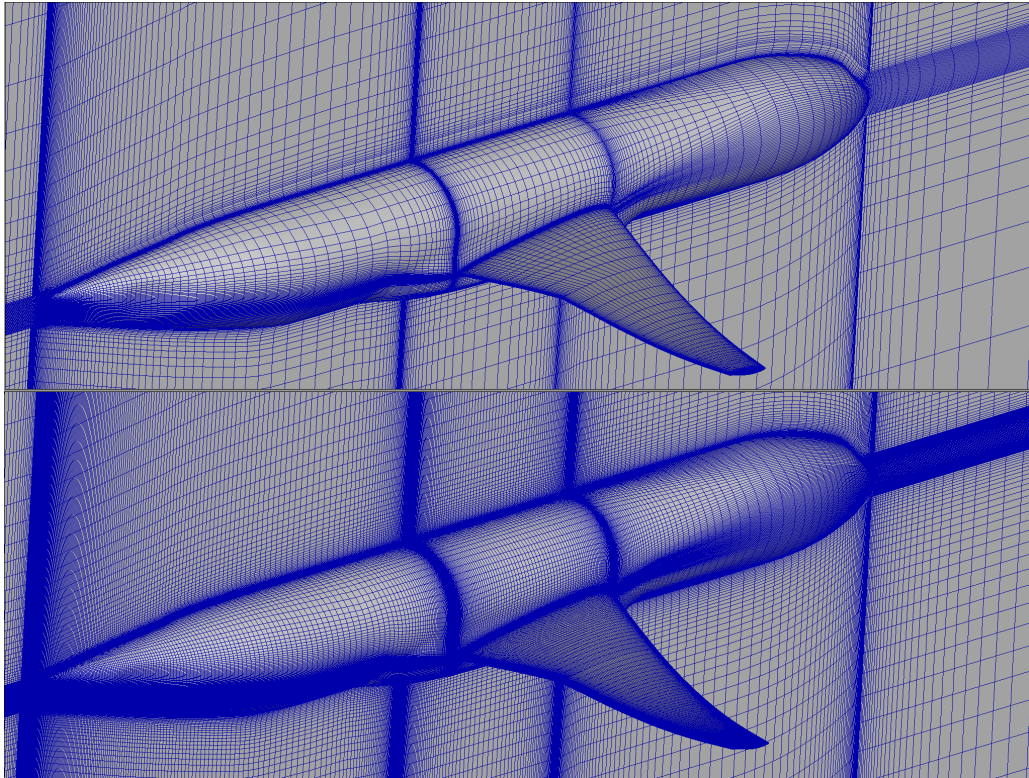
Figure 1 – NASA CRM surface and symmetry plane coarse (5 million cells) and baseline (45 million cells) grids.

Table 1 – NASA CRM CFD grids provided by Ref. [10] to the 6th DPW and used for the present study.

Grid Name	Grid Size
Very Coarse	5×10^6 cells
Medium (Baseline)	45×10^6 cells

2.1.2 HIRENASD Aerodynamic Model

In Ref. [2], the present authors reported the application of BRU3D-FSI process to the HIRENASD model considering the three levels of CFD grid refinement shown in Fig. 2. These grids were made available by ANSYS at the time of the 1st AIAA Aeroelastic Prediction Workshop (AePW-1) [12]. The grid sizes are indicated in Table 2.

Table 2 – HIRENASD grids available for the AePW-1 [12].

Grid Name	Grid Size
Grid 1	3×10^6 cells
Grid 2	10×10^6 cells
Grid 3	28×10^6 cells

The numerical domain to be considered in the present work consists in a block-structured hexahedral volumetric grid with quadrilateral surface mesh as shown in Fig. 1. Both CFD General Notation System (CGNS) and blocking data were made available by ANSYS Germany for the 1st AIAA Aeroelastic Prediction Workshop [12]. These grids are refined enough to achieve the boundary layer discretization for $Y^+ \leq 1$, according to the Reynolds number range tested in the European Transonic Wind Tunnel (ETW), as presented in Table 2.
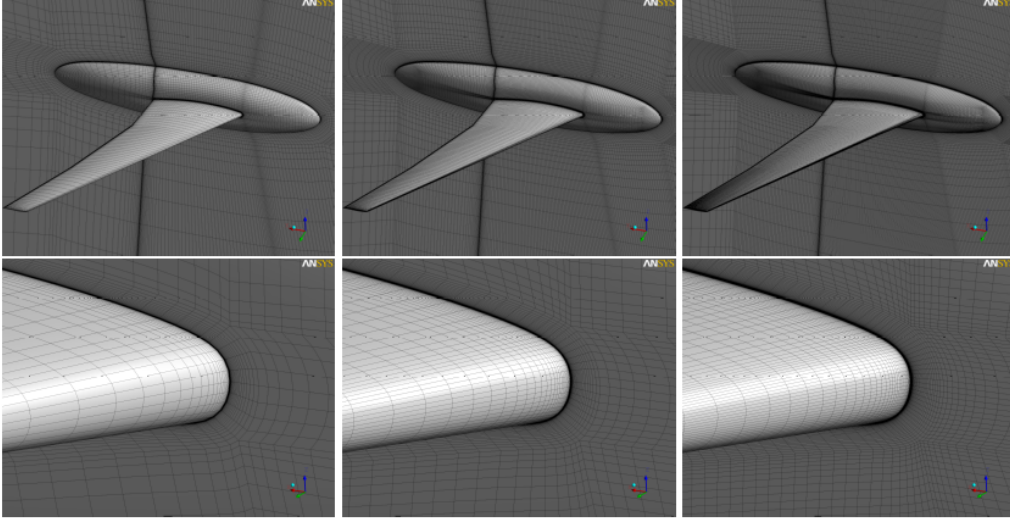
Figure 2 – HIRENASD structured surface grids in perspective view for the three refinement levels [12].

2.2 Structural Modeling

The system of equations governing the linear structural dynamics response can be obtained through the Hamilton Principle which, according to Ref. [9], states that

$$\int_{t_1}^{t_2} (\delta L + \delta W)dt = 0 \qquad , \text{ where } \qquad L = T - V \ . \tag{5}$$

Associating Hamilton's Principle with the finite element discretization of the structural domain, the equations of motion are obtained in the form

$$\mathbf{M\ddot{U}}(t) + \mathbf{C\dot{U}}(t) + \mathbf{KU}(t) = \mathbf{R}(t) \ , \tag{6}$$

where $\mathbf{M}$ is the mass matrix, $\mathbf{C}$ is the viscous damping matrix, $\mathbf{K}$ is the stiffness matrix, $\mathbf{U}(t)$ is the vector of generalized displacements, and $\mathbf{R}(t)$ is the vector of generalized forces. When dynamic effects are neglected, Eq. (6) can be reduced to a static equilibrium equation of the form

$$\mathbf{KU} = \mathbf{R} \ . \tag{7}$$

In order to perform the modal projection, the eigensolutions of the associated undamped structure are first computed by solving the following eigenvalue problem:

$$(\mathbf{K} - \omega_i^2 \mathbf{M})\phi_i = \mathbf{0} \ , \tag{8}$$

where ω_i are the natural frequencies and ϕ_i denote the corresponding natural vibration modes. The displacement field is, then, expressed as a linear combination of the vibration mode shapes as

$$\mathbf{U} = \sum_{i=1}^{n} q_i \phi_i = \Phi \mathbf{q} \ . \tag{9}$$

Associating Eqs. (7) and (9), and making use of the orthogonality properties of the eigenvectors, one obtains the following solution for the reduced problem

$$\mathbf{q} = \Lambda^{-1} \Phi^T \mathbf{R} \ , \tag{10}$$

where $\Lambda = diag\{\omega_1^2 ... \omega_n^2\}$ is the spectral matrix and $\Phi = [\phi_1 ... \phi_n]$ is the modal matrix. Therefore, the static structural problem becomes dependent of the natural frequencies and associated modal shapes. Moreover, the aerodynamic forces applied on the wing surfaces elements are projected into those modes.

2.2.1 NASA CRM Structural Model

The NASA CRM structural model was described in Ref. [13] and the finite-element structural model is shown in Fig. 3a. This 4-node tetrahedral FEM model represents the wing, fuselage and horizontal tail, and it excludes pylons and nacelles for this case. The FEM model has approximately 1×10^6 nodes and 8×10^6 degrees of freedom.
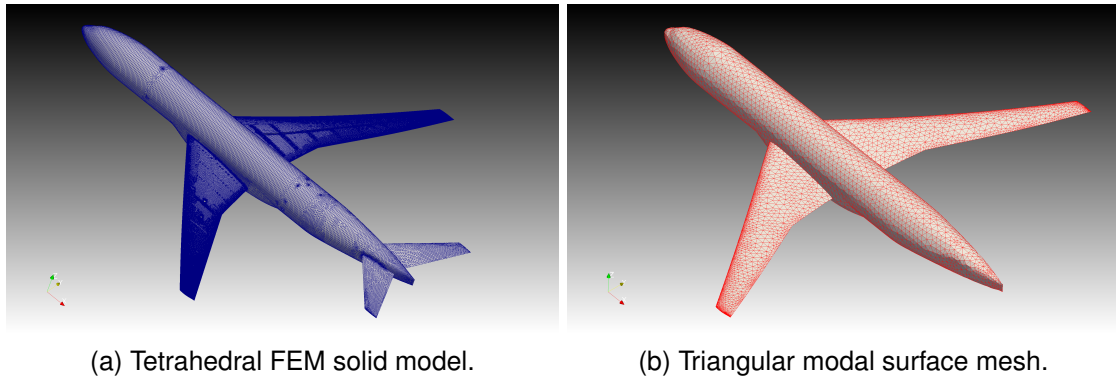

(a) Tetrahedral FEM solid model.

(b) Triangular modal surface mesh.

Figure 3 – NASA CRM unstructured solid dynamic grid.

This fine FEM model was reduced to a modal representation as performed by the Ref. [3, 10]. This surface mesh, shown in Fig. 3b, has only 1×10^4 nodes and it only represents the wing and body surface, as the horizontal tail is not considered in the DPW-6 aerostructural test case.

2.2.2 HIRENASD Structural Model

The HIRENASD structural domain to be numerically modeled is also provided by the AePW-1 website [12] and it consists in a FEM unstructured tetrahedral grid, shown in Fig. 4a. The structural model comprises the wing, the excitation transmission system and the clamping flange for the main balance connection. The FEM model has approximately 1×10^5 tetrahedral elements with quadratic shape functions.

(a) Tetrahedral FEM solid model.
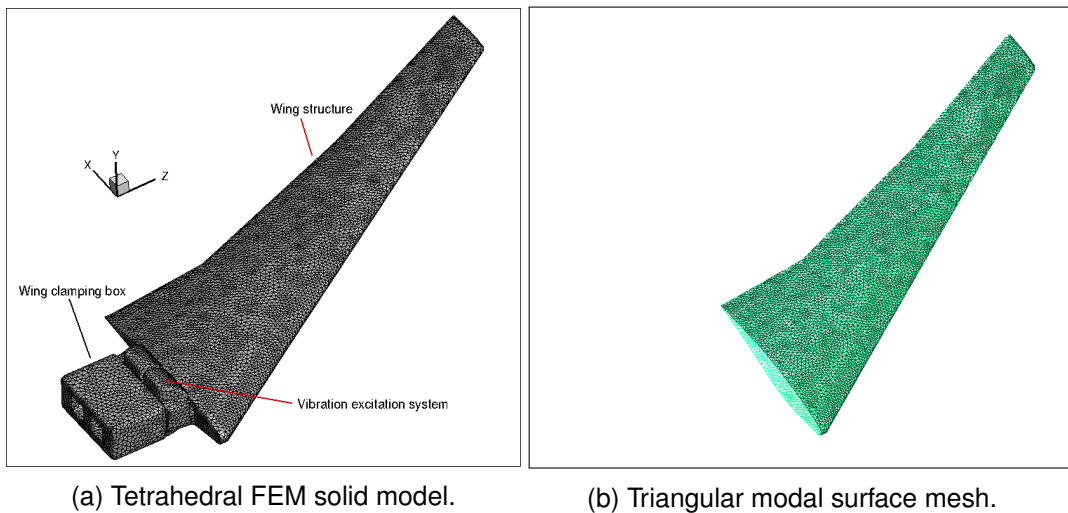
(b) Triangular modal surface mesh.

Figure 4 – HIRENASD structural solid model and modal displacement surface mesh representation.

The modal base for this configuration was obtained using the MSC NASTRAN solver and the original FEM model previously described. The modal displacements are represented for the present simulations using approximately 1×10^4 wing surface mesh nodes, which are shown in Fig. 4b. One can observe in the figure that the excitation transmission system and the clamping flange for the main balance connection are not included in this surface mesh representation. As the excitation system and main balance are considered highly rigid and they are located inside the body fuselage, the

modal displacement results from their nodes are not considered for mesh morphing in the present simulations. A study of wing tip displacement convergence, for a given load, as a function of the number of mode shapes is present in Ref. [11]. The results there reported indicate that the use of the first 10 flexible mode shapes for the HIRENASD model can be considered acceptable for the static aeroelastic calculations.

2.3 Fluid-Structure Integration

The complete static aeroelastic analysis process is illustrated in Fig. 5. The initial aerodynamic loads are obtained by performing CFD simulations with the unloaded wing shape. The calculation is advanced until convergence of the aerodynamic forces for this configuration and, hence, the determination of the rigid configuration aerodynamic response. As previously indicated, aerodynamic calculations use the BRU3D solver, and all simulations were performed in the CeMEAI cluster [15]. The wing pressure distribution results are, then, interpolated from CFD centroid surface elements to superficial structural nodes using the Constant Strain Triangle (CST) method [14]. In the next of the process, the wing structural surface node displacements are obtained from the finite element modal basis approach and, then, they provided to the fluid mesh morphing process by imposing the wing deflection shape. Wing aerodynamic mesh nodes are displaced accordingly and, then, such displacements are propagated to the volume grid using a Radial Basis Function (RBF) approach. The process, as indicated in Fig. 5, is then repeated until the aeroelastic equilibrium is reached.
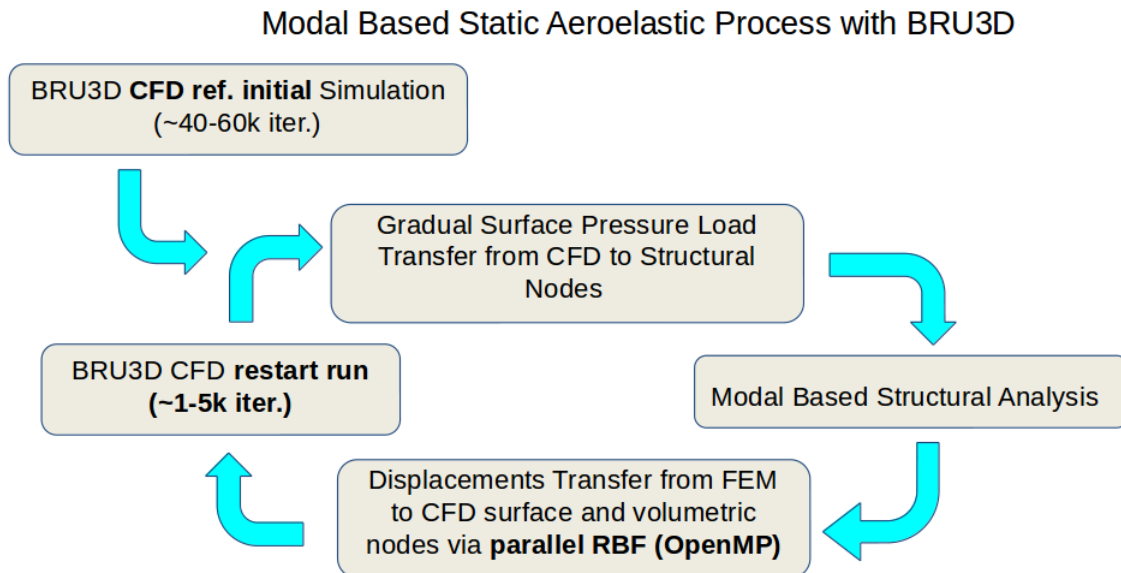
Modal Based Static Aeroelastic Process with BRU3D

Figure 5 – Static aeroelastic computational FSI processes.

2.3.1 Load Transfer

The distributed aerodynamic pressure generated by the CFD simulations must be transferred to the finite element model degrees of freedom preserving the integral loads. Therefore, considering that the CFD code uses a 2nd-order finite volume method with constant pressure values along the faces of the cells, a first step is to integrate forces on each surface of the fluid cell, creating air load vectors. In a second stage, the process finds the structural element centroid which is the nearest centroid to the centroid of the aerodynamic cell face. This structural model cell receives the loads from that particular fluid cell. The implemented process, then, uses the CST shape function formulation to distribute the CFD air load to the finite element surface nodes. This method follows the so-called "area coordinate approach" presented in Ref. [14].

2.3.2 Fluid Mesh Morphing

Radial basis functions (RBFs) are widely used for multivariable interpolation. In the present work, a RBF-based numerical FORTRAN code, also developed in-house, is used for fluid mesh morphing.

The implemented RBF formulation follows the approach presented in Refs. [17, 18, 19], in which a node displacement calculated during the structural analysis can be approximated by a sum of basis functions as

$$d_i(x) = \sum_{j=1}^{Nb} \alpha_j \phi(||x - x_{bj}||) + p_t(x) \ . \tag{11}$$

The Wendland compactly supported functions are used, as recommended in Ref. [17]. Moreover, the system of equations for RBF calculation has to be defined in three directions, *i.e.*, $\mathbf{d}_i(x) = [\Delta\mathbf{x}, \Delta\mathbf{y}, \Delta\mathbf{z}]$, for the calculation of the α_x, α_y and α_z coefficients. Therefore, three linear systems of equations are solved using the GMRES method [16]. After this first stage of calculations, the volume mesh, indicated by the v subscript, is updated using the aero-structural $\mathbf{A}$ matrix as

$$\Delta\mathbf{x}_v = \mathbf{A}\alpha_x \ . \tag{12}$$

The same procedure is performed for the y and z directions. Due to the large size of the $\mathbf{A}$ matrix, when a fine CFD mesh is used, this procedure is performed in a parallel fashion using Open Multiprocessing (OpenMP) in the RBF code.

3. Results

3.1 HIRENASD Model

As proposed in this work, a study of grid refinement using the HIRENASD model is presented in this section considering both purely aerodynamic simulations, using the BRU3D, and static aeroelastic simulations, where the BRU3D is coupled with a structural solution using a linear modal basis, and load and displacement transfer methods presented above. These CFD grids were made available by ANSYS at the time of the 1st AIAA Aeroelastic Prediction Workshop (AePW-1) [12]. The grid sizes are indicated in Table 2. The flight condition considered for this comparison is freestream Mach number $M_\infty = 0.80$, Reynolds number $Re = 7 \times 10^6$, dynamic pressure $q_{dyn}/E = 0.22 \times 10^{-6}$ and angle of attack $\alpha = 1.5$ deg.

3.1.1 Wing Deflection

Considering the static aeroelastic simulations, Fig. 6 presents the spanwise wing deflection results for the 3 CFD grid levels presented in Table 1. The FSI simulations with the grid levels 1 and 2 were performed using the SST turbulence model for the aerodynamic solution, whereas the simulation with the finest grid was performed considering both the SST and SA turbulence models. In the figures, the black square represents the experimental data for wing bending and twist deflection from Ref. [6]. The triangle, upside-down triangle and the diamond symbols represent the BRU3D-FSI results using grids 1 to 3 with the SST turbulence model. And, the vertical dash represents the BRU3D-FSI results using grid 3 and SA turbulence model.

Analyzing curves Figs. 6a and 6b, a very similar behavior in both bending and twist deflections are noticed for all present numerical results, where differences are concentrated only in wingspan greater than 1 meter. The Figs. 6c and 6d focus on the wing tip results. As the grid is refined a slightly increase in wing deflection is noticed. The differences in wing tip displacements between the results with the three different grids are quite small, amounting to less than 1 mm in the bending displacement and on the order of 0.1 deg. for the twist. In addition, the wing bending results with the SA model shows a small reduction in the wingtip deflection when compared with SST model results, but within the same order of magnitude already reported. And, in general, the numerical results show a slightly greater wing deflection than the experimental results.

3.1.2 Aerodynamic Coefficients

Using the AePW-1 participant results and computational results from different solvers reported by Ref. [6] as reference data, the present rigid aerodynamic and static aeroelastic simulation results in terms of lift, C_L, drag, C_D, and pitching moment, C_M, coefficients are plotted in Figs. 7a, 7b, and 7c. The authors are particularly interested in the effects of grid refinement and the relative behavior of the present simulations as compared to the aerodynamic data available. The other computational results reported in these figures, referenced as "AePW participants" in the plots, were obtain from AePW data

(a) Bending, in m.

(b) Twist, in deg.

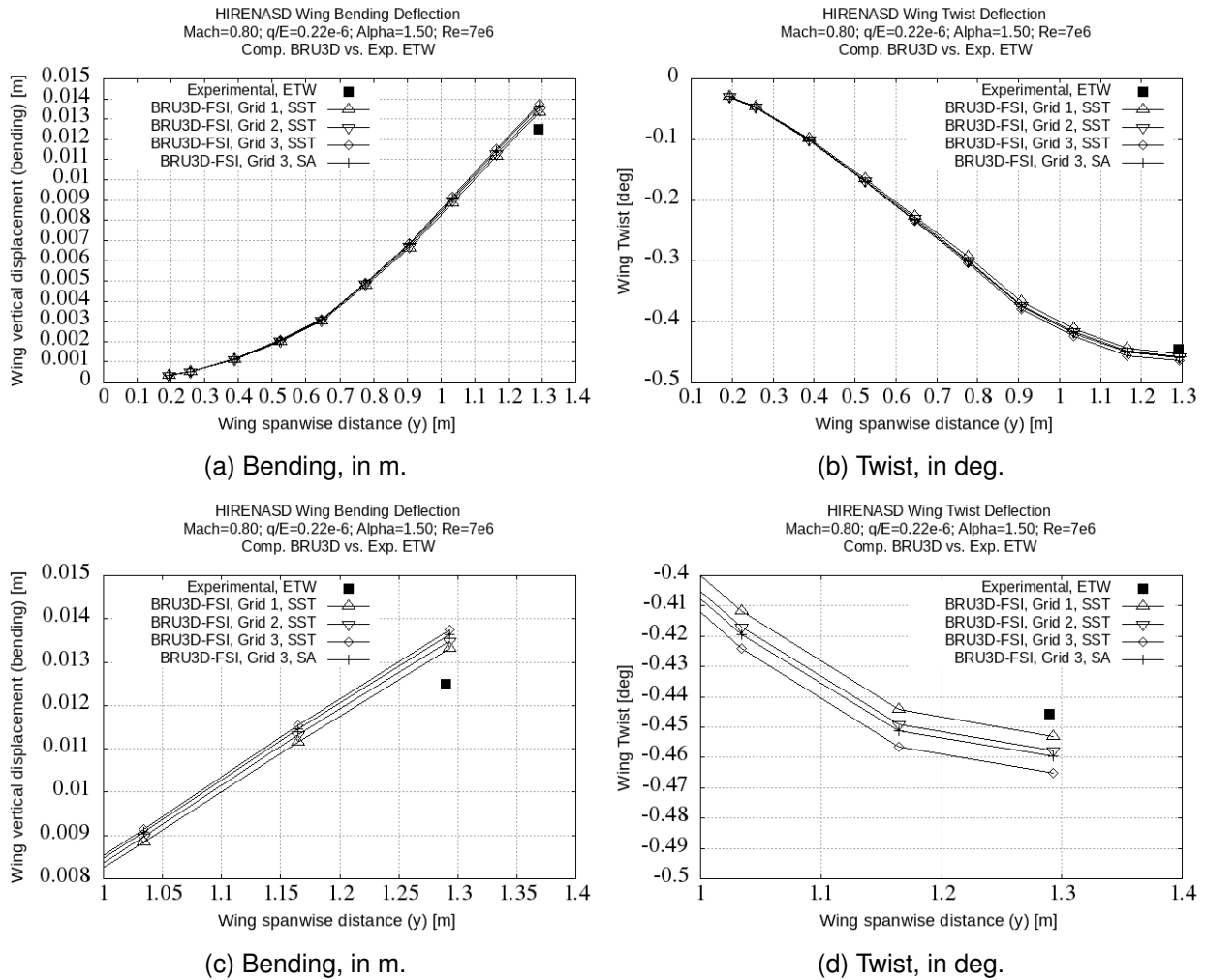(c) Bending, in m.

(d) Twist, in deg.

Figure 6 – HIRENASD wing deflection for $M_\infty = 0.80$, $Re = 7 \times 10^6$ and $q_{dyn}/E = 0.22 \times 10^{-6}$.

where different turbulence models and grid systems were used. Finally, the results reported in the figures that are labeled as "BRU3D-CFD" refer to purely aerodynamic simulations for the initial rigid configuration, whereas those labeled as "BRU3D-FSI" refer to static aeroelastic present calculations using the process described in this paper.

An assessment of the present aerodynamic coefficient results, when compared to the various calculations included in Fig. 7a, indicates that the inclusion of static aeroelastic effects, for any given aerodynamic grid, has a tendency of bringing our results into the same range as the reference data or, at least, much closer to the range of C_L's computed by other groups. And, the present aerostructural calculations using grid 3 shows converged result when compared with grid 2 previous published results. Moreover, SST and SA turbulence models simulations achieved practically the same value of C_L.

Figure 7b presents a similar comparison for the drag coefficient as a function of grid refinement. One can clearly observe that, in relative terms, the inclusion of wing flexibility in the simulations has a much smaller effect on the values of drag coefficient computed, for a given grid, than one would see for the lift coefficient in Fig. 7a. In the drag coefficient calculations, the inclusion of static aeroelastic effects has a tendency of also bringing our results towards the range of values obtained by the other groups, but, for the most part, it is still predicting drag coefficient values which are considerably larger than those obtained in the reference data. The drag coefficient trends observed with grid refinement in the present calculations is similar with those observed for lift coefficient, where the results for grid 3 confirms the values obtained with grid 2 even when SA turbulence model is used.

Finally, results for the pitching moment coefficient are reported in Fig. 7c. The present aerostructural calculations using grid 3 with SST and SA turbulence models also confirms the results obtained with

grid 2. As already showed for lift and drag coefficients, BRU3D-FSI results have a slightly difference with numerical data reported by Ref. [6], but keeping C_M results within AePW participants results. Moreover, the inclusion of aeroelastic effects has a tendency of making C_M values less negative, for a given grid, which is the expected result as the wing twist will certainly contribute to alleviate the aerodynamic loads acting on the structure.
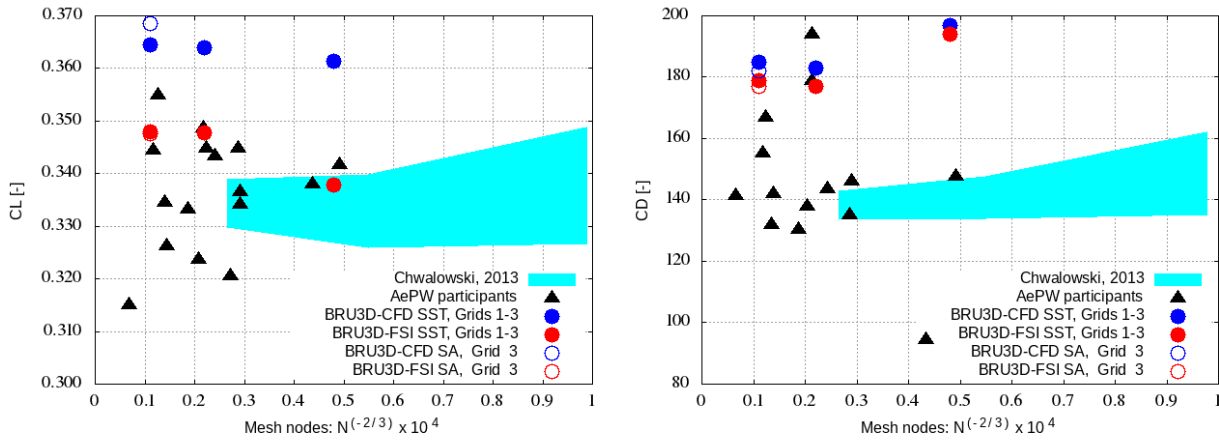
(a) Lift Coefficient

(b) Drag Coefficient
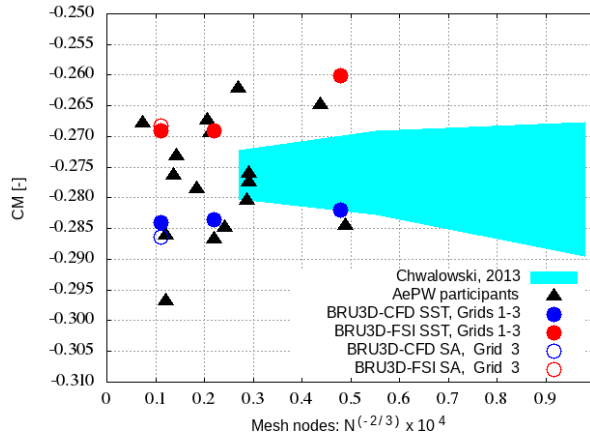
(c) Pitching Moment Coefficient

Figure 7 – The HIRENASD aerodynamic coefficient comparisons for $M_\infty = 0.80$, $Re = 7 \times 10^6$ and $q_{dyn}/E = 0.22 \times 10^{-6}$.

3.1.3 Pressure Distributions

Figure 8 presents the pressure coefficient distributions at three different spanwise stations at $y = 0.1845$ m, $y = 0.5845$ m and $y = 1.2240$ m, which correspond, respectively, to a wing root, mid-span and a station near the wing tip region for the HIRENASD model. The flight Mach number is $M_\infty = 0.80$ and the angle of attack is $\alpha = 1.5$ deg. These figures compare the present computational static aeroelastic results for grid 3 with previous computed data from Ref. [2]. The present computational results are also compared to the experimental data for $q_{dyn}/E = 0.22 \times 10^{-6}$ and $Re = 7 \times 10^6$.

Comparing the pressure coefficient distributions in these 3 wing sections, two important facts raise. The first, noticed in the wing root and mid-span sections, shows a slightly stronger shock wave in both the upper and lower surfaces of the wing in the results from CFD grids 2 and 3 when compared with those from CFD grid 1 and the experimental data. Although this may seem to be a discrepancy with experimental results, the two finest grids have very similar results to each other, which can indicate a convergence trend in terms of CFD mesh refinement. On the other hand, observing the results close to the wing tip, where there is no presence of a strong shock wave, all three grids bring very close results, indicating no local effect of grid refinement on the wing pressure distribution coefficient.
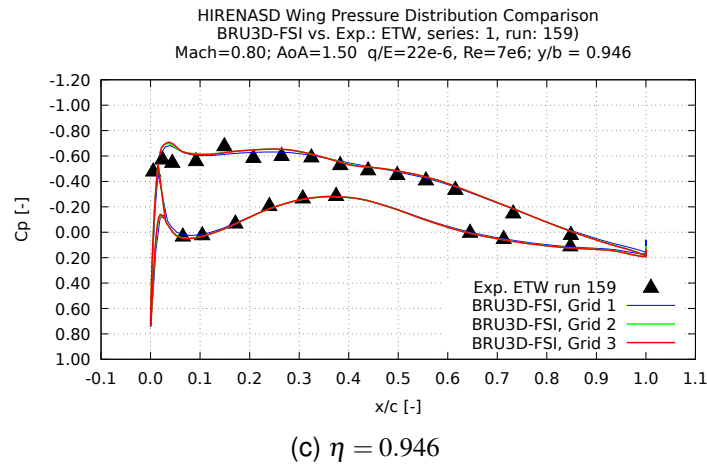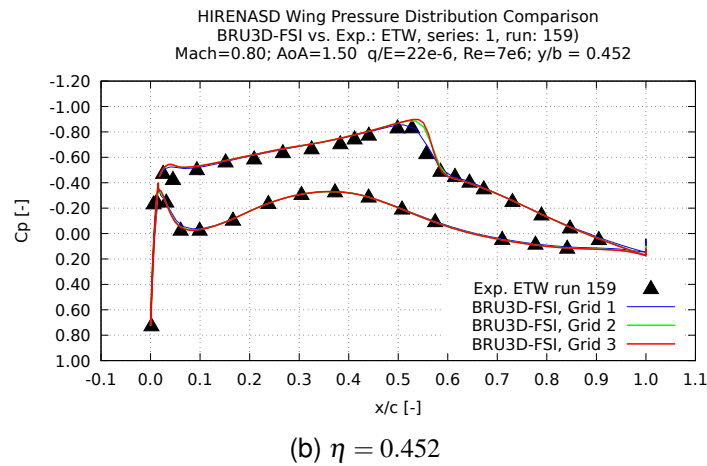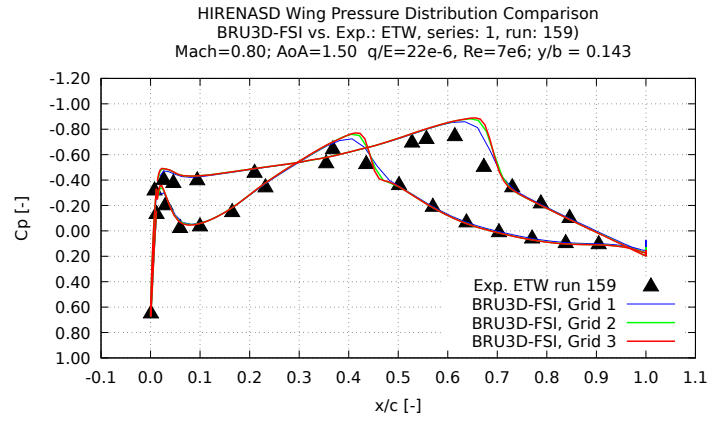
HIRENASD Wing Pressure Distribution Comparison
BRU3D-FSI vs. Exp.: ETW, series: 1, run: 159)
Mach=0.80; AoA=1.50 q/E=22e-6, Re=7e6; y/b = 0.143

(a) $\eta = 0.143$

HIRENASD Wing Pressure Distribution Comparison
BRU3D-FSI vs. Exp.: ETW, series: 1, run: 159)
Mach=0.80; AoA=1.50 q/E=22e-6, Re=7e6; y/b = 0.452

(b) $\eta = 0.452$

HIRENASD Wing Pressure Distribution Comparison
BRU3D-FSI vs. Exp.: ETW, series: 1, run: 159)
Mach=0.80; AoA=1.50 q/E=22e-6, Re=7e6; y/b = 0.946

(c) $\eta = 0.946$

Figure 8 – Comparisons of the HIRENASD pressure coefficient distributions along the span at
$M_\infty = 0.80$, $Re = 7 \times 10^6$, $q/E = 0.22 \times 10^{-6}$.

3.2 NASA CRM Model

The first application of BRU3D-FSI process to the NASA CRM model is described in Ref. [11], where the wing displacement results obtained for two modal base sizes, 10 and 16 flexible modes, were similar with those obtained by the 6th AIAA DPW participants [5] with maximum twist deviations of about 0.1 deg. at the wing tip in comparison with both wind tunnel results and DPW participants. Although both root and wing tip regions presented quite acceptable correlations between calculated and experimental data in the pressure distributions, some discrepancies were observed at mid span stations of the wing that may be related with the use of a CFD grid with 5 million cells. To address with this discrepancies, here in this work a finer CFD grid level is considered. Figure 1 and Table 1

present data for the coarse and baseline grids used here, where the baseline has the equivalent level with those used by 6th DPW participants for the aeroelastic test case 5.

3.2.1 Wing Deflection

The NASA CRM wing displacements, in terms of bending and twist, are the focus of test case 5 from the 6th DPW. The ETW experimental data and participant results are published in Ref. [5]. These results are used here as the reference data in order to verify the capability of the BRU3D-FSI framework for predicting static aeroelastic effects. Figures 9a and 9b present the comparisons of wing displacements for the present calculations using the two levels of CFD grid refinement, and compares with the reference data. It is interesting to observe that, to a great extent, the present calculations fall within the dispersion of the results from the workshop participants. One must observe that in Fig. 9a the present calculation using the baseline grid clearly improve the results approaching the experimental data. However, using a modal base with 16 flexible modes, red curve, it is observed that Fig. 9b shows an increase in wing tip twist prediction when the CFD grid is refined from 5 to 45 million cells. And, a additional simulation using the CFD grid with 45 million cells and a structural modal base with 34 modes, green curve, keeps the twist results with DPW data range.
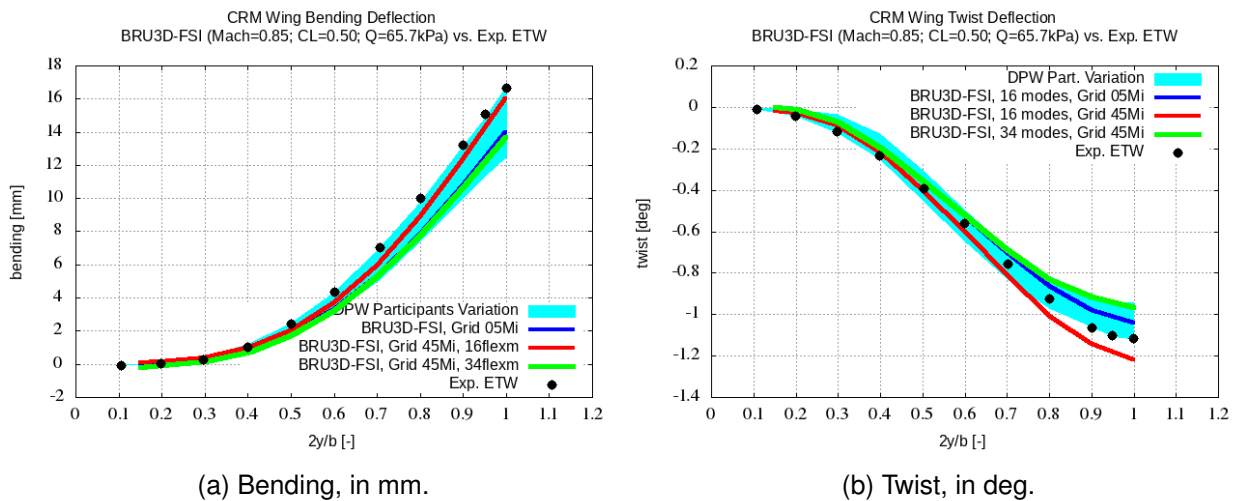

(a) Bending, in mm.

(b) Twist, in deg.

Figure 9 – NASA CRM wing deflection for $M_\infty = 0.85$, $Re = 5 \times 10^6$ and $q_{dyn} = 65kPa$.

3.2.2 Aerodynamic Coefficients

Figure 10 presents the comparison between BRU3D-FSI present results for baseline CFD grid, DPW6 Case 5 participants and NTF Wind Tunnel data using Wing-Body configuration at the same specified flow condition, $CL = 0.050$, $Mach = 0.85$, $Q = 65kPa$, in terms of alpha, drag, and pitching moment coefficient. Although all computed results present good agreement, it is very encouraging that the BRU3D-FSI results are closer to the experimental ETW data. The DPW-6 participants are represented by the blue bars using the same label codes presented by the [5]. And, the present BRU3D-FSI results using baseline CFD grid are represented by red and green bars, respectively, for 16 and 34 flexible modes.

Here, it is possible to notice a good correlation between the obtained results in front to the reference data in terms of angle of attack, drag moment and pitching moment coefficient. Despite the expected result was improve the correlation when a lager modal base is considered, the opposite was obtained. So, even with both FSI simulations presenting acceptable results, a dedicated study of sensitivity to the size of the modal base still necessary.

An important fact is noticed when comparing the correlation of the aerodynamic drag coefficients obtained for both NASA CRM and HIRENASD models. The HIRENASD model results, from previous sections, showed drag coefficient values greater than the reference data by approximately 20 drag counts. And, considering the NASA CRM model, that was design for drag prediction analysis and

uses C_L driver input parameter instead of angle of attack, the difference between obtained values and experimental data is smaller than 5 drag counts.
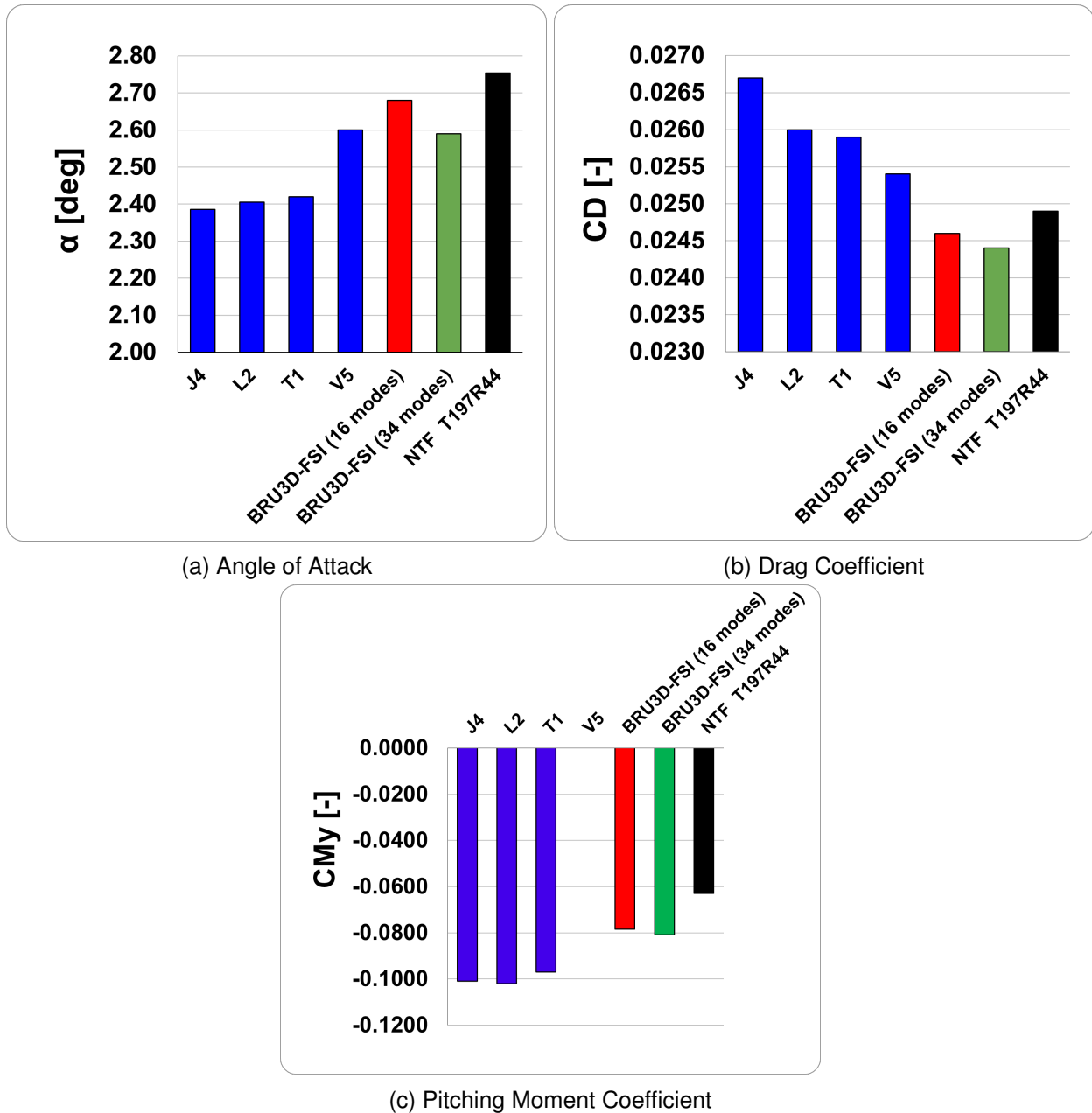

(a) Angle of Attack

(b) Drag Coefficient

(c) Pitching Moment Coefficient

Figure 10 – The NASA CRM aerodynamic coefficient comparisons for $M_\infty = 0.85$, $Re = 5 \times 10^6$ and $q_{dyn}/E = 0.36 \times 10^{-6}$.

3.2.3 Pressure Distributions

Figure 11 shows the wing pressure coefficient distribution comparisons for different stations along wing span obtained from the BRU3D-FSI framework and experimental data from Nasa Transonic Facilities, NTF, from Ref. [20]. The solid blue curves indicate results for the coarse grid, the green curves are the present FSI result using 45 million CFD cells and 16 flex modes, and red curves are the present FSI result using 45 million CFD cells and 34 flex modes.

The main differences between numerical results from coarse grid and experimental results observed in Ref. [11] appear to be improved with the baseline grid, approaching the experimental data due to a better shock wave prediction. With the use of the baseline grid, a clear improvement in the prediction of both shock wave position and wing trailing edge pressure distribution can be noticed. This effect leads to a better prediction of drag and pitching moment coefficients, which are fundamental in a wind

tunnel campaign. And, it shows that the BRU3D-FSI process is capable of obtaining results equivalent to those from transonic wind tunnel tests under typical cruising conditions, even with structural flexibility effects on the wind tunnel model wings.
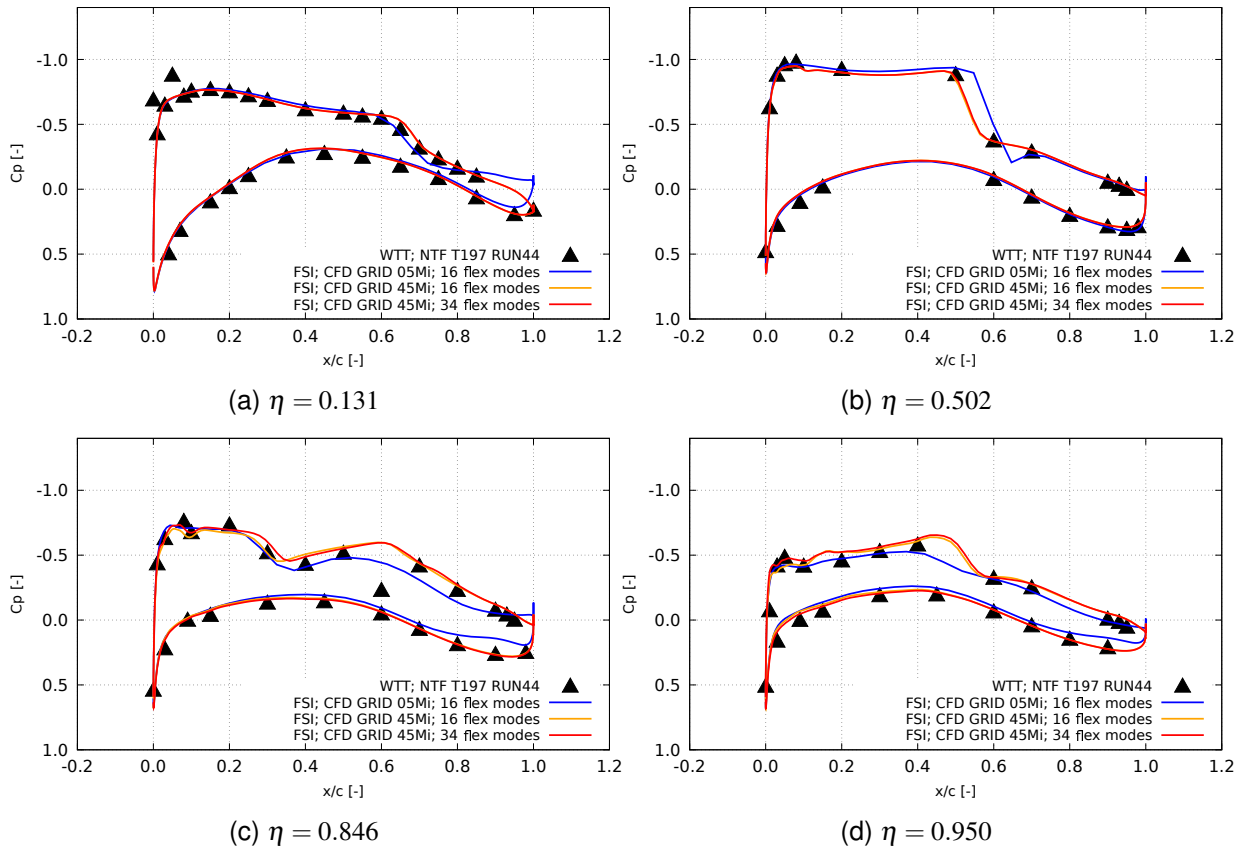

(a) $\eta = 0.131$

(b) $\eta = 0.502$

(c) $\eta = 0.846$

(d) $\eta = 0.950$

Figure 11 – Comparisons of the NASA CRM pressure coefficient distributions along the span at $M_\infty = 0.85$, $Re = 5 \times 10^6$, $Q = 65kPa$.

4. Final Remarks

In the present work, the effects of aerodynamic and structural model improvements are presented and discussed. The static aeroelastic analysis process proved to be robust when using refined CFD grids in the order of 30 to 45 million cells. The results obtained for the HIRENASD model demonstrate that the use of CFD grids levels 2 and 3 achieves convergence of the aerodynamic response, despite the discrepancy in terms of drag coefficient by approximately 20 drag counts when compared to the experimental results. The observation of the pressure distributions indicates that there is a slight increase in the level of the shock wave on the wing as the grid is refined. Furthermore, a comparison of results obtained with the SST and SA turbulence models is presented. The overall conclusion is that similar aerodynamic results are obtained, despite some slight differences in the aerodynamic coefficients for the finest grid and also in terms of wing deflection. Hence, the turbulence models used do not have a major impact in the flowfields addressed here.

The NASA CRM aerostructural computations have shown a clear improvement in both pressure distributions and integrated aerodynamic coefficients when using the 45 million cell CFD grid. The fine grid results are in much closer agreement with the experimental data. Despite the fact that the NASA CRM FSI simulations presented a considerable improvement, a more detailed study concerning the size of the CRM modal base is still necessary. In a similar fashion, there is also need to further explore aspects related to the structural flexibility of the aerostructures considered, in order to more closely resemble the actual properties found in real aircraft structures.

5. Acknowledgments

6. Contact Author Email Address

Mail to: j.allanantunes@gmail.com
Mail to: joaoluiz.azevedo@gmail.com

7. Copyright Statement

References

[1] Kroll N, Heinrich R, Krueger W and Nagel B. Fluid-Structure Coupling for Aerodynamic Analysis and Design: A DLR Perspective - Invited. *46th AIAA Aerospace Sciences Meeting and Exhibit*, Reno, Nevada, USA, 2008.

[2] Lyrio J, Azevedo J, Rade D, da Silva R and Breviglieri C. Assessment of a Framework for Static Aeroelastic Response Calculations in Transonic Flows. *AIAA Aviation Forum*, Virtual Event, 2021.

[3] Lyrio J, Azevedo J, Rade D, da Silva R and Breviglieri C. Static Aeroelastic Computations of Wing Configurations in Transonic Flows at High Reynolds Numbers. *32nd Congress of the International Council of the Aeronautical Sciences*, Shanghai, China, 2021.

[4] Vassberg J, M Dehaan, rivers M, Wahls R. Development of a Common Research Model for Applied CFD Validation Studies. *26th AIAA Applied Aerodynamics Conference*, Honolulu, HI, USA, 2008.

[5] Keye S and Mavriplis D. Summary of Case 5 from Sixth Drag Prediction Workshop: Coupled Aerostructural Simulation. *Journal of Aircraft*, Vol. 55, No. 4, pp 1380-1387, 2018.

[6] Chwalowski P, Heeg J, Dalenbring M, Jirasek A, Ritter M and Hansen T. Collaborative HIRENASD Analyses to Eliminate Variations in Computational Results. *The International Forum on Aeroelasticity and Structural Dynamics*, Bristol, United Kingdom, 2013.

[7] Junqueira-Junior C, Azevedo J, Scalabrin L and Basso E. A Study of Physical and Numerical Effects of Dissipation on Turbulent Flow Simulations. *Journal of Aerospace Technology and Management*, Vol. 5, No. 2, pp 145-168, 2013.

[8] da Silva R, Azevedo J. Numerical Simulations of Turbulent Flows Over the ONERA-M6 And DLR-F6 Configurations. *30th Congress of the International Council of the Aeronautical Sciences*, Daejeon, Korea. 2016.

[9] Craig R and Kurdila A. *Fundamentals of Structural Dynamics*. 2nd edition, John Wiley and Sons, 2006.

[10] de Souza R, Mestriner M, de Souza M, Ferrari M, Breviglieri C and Spode C. Aerodynamic and Static Aeroelastic Numerical Simulations for the 6th AIAA CFD Drag Prediction Workshop. *AIAA Aviation Forum*, Washington, DC, 2016.

[11] Lyrio J, Azevedo J, Rade D and da Silva R. Computational Static Aeroelastic Analyses in Transonic Flows. *AIAA Aviation Forum*. Virtual Event, 2020.

[12] Hansen, T. HIRENASD coarse structured grid, Aeroelastic Prediction Workshop. *Aeroelastic Prediction Workshop, AePW-1*. Available in: https://c3.ndc.nasa.gov/dashlink/resources/381/. in 2022-05-25.

[13] Keye S, Rudnik R. Validation of Wing Deformation Simulations for the NASA CRM Model using Fluid Structure Interaction Computations. *53rd Aerospace Science Meeting*. Kissimmee, Florida, USA, AIAA 2015-0619, 2015.

[14] Guruswamy G. A Review of Numerical Fluids/Structures Interface Methods for Computations Using High-Fidelity Equations. *Computers and Structures*. Vol. 80, No. 1, pp 31-41, 2002.

[15] CeMEAI. Center for Mathematical Sciences Applied to Industry. http://www.cemeai.icmc.usp.br/.

[16] Saad Y. *Iterative Methods for Sparse Linear Systems*. 2nd edition, Society for Industrial and Applied Mathematics, 2003.

[17] Beckert A and Wendland H. Multivariate Interpolation for Fluid-Structure-Interaction Problems Using Radial Basis Functions. *Aerospace Science and Technology*. Vol. 5, No 2, pp 125-134, 2001.

[18] de Boer A, van der Schoot M and Bijl H. New Method for Mesh Moving Based on Radial Basis Function Interpolation. *European Conference on Computational Fluid Dynamics, ECCOMASS CFD*. Egmond aan Zee, NL, 2006.

[19] Rendall T and Allen C. Efficient Mesh Motion Using Radial Basis Functions with Data Reduction Algorithms. *Journal of Computational Physics*, Vol. 228, No. 17, pp 6231-6249, 2009.

[20] NASA Common Research Model. NATIONAL TRANSONIC FACILITY RESULTS. Available in: https://commonresearchmodel.larc.nasa.gov/experimental-data/ntf-experimental-results/